water

MDPI

Article

The Hydrochemistry Characteristics and Chemical Weathering Intensity of an Anthropogenically Involved Catchment, South China

Fan Liu [1,2,3,4,5,6], Song Wang [7], Jia Wang [1,2,4,5,*], Fang Guo [1,2,3,4,*], Shi Yu [1,2,3,4] and Ping'an Sun [1,2,3,4]

1 Key Laboratory of Karst Dynamics, MNR & GZAR, Institute of Karst Geology, Chinese Academy of Geological Sciences, Guilin 541004, China; liufancags@126.com (F.L.); yushihydrogeo@163.com (S.Y.); sunpingan@mail.cgs.gov.cn (P.S.)
2 International Research Centre on Karst under the Auspices of UNESCO, National Center for International Research on Karst Dynamic System and Global Change, Guilin 541004, China
3 Guilin Karst Geology Observation and Research Station of Guangxi, Guilin 541004, China
4 Pingguo Guangxi, Karst Ecosystem, National Observation and Research Station, Pingguo 531406, China
5 Guangxi Karst Resources and Environment Research Center of Engineering Technology, Guilin 541004, China
6 School of Water Resources and Environment, China University of Geosciences, Beijing 100083, China
7 Guangdong Hydrogeology Battalion, Guangzhou 510510, China; wangsong2002110@163.com
* Correspondence: karst_jia@163.com (J.W.); gfkarst@126.com (F.G.)

Abstract: The hydrochemical characteristics of watersheds are influenced by many factors, with chemical weathering and human activities exerting the most substantial influence. Performing a quantitative evaluation of the factors contributing to the chemical weathering of rocks is of significant scientific importance. This research zeroes in on the Qingtang River basin to elaborate on the hydrochemical characteristic, explore the origins of ions, and quantify the influence of anthropogenic discharges amidst cation interferences, thus improving the accuracy of chemical weathering rate estimations. The samples encompassed surface water, groundwater, and water from dripping in karst caves. The findings indicate that human-induced alterations significantly influence hydrogeochemical dynamics, although chemical weathering of rocks in their natural state is the controlling factor. The mean contributions of cations from atmospheric deposition, human inputs, carbonate weathering, and silicate weathering were 17.56%, 21.05%, 51.77%, and 9.54%, respectively. The chemical weathering rate for carbonate rocks was 62.4 $t \cdot km^{-2} \cdot a^{-1}$, which increased by 27.87% due to the influence of exogenous acids. The anthropogenic impact is predominantly evident in two aspects: (1) the alteration of hydrochemical processes within the watershed through direct input of ions, and (2) the acceleration of rock weathering rates in the watershed due to the exogenous acids.

Keywords: chemical weathering; hydrogeochemistry; ion source; carbonate and silicate catchment; anthropogenic activities

Citation: Liu, F.; Wang, S.; Wang, J.; Guo, F.; Yu, S.; Sun, P. The Hydrochemistry Characteristics and Chemical Weathering Intensity of an Anthropogenically Involved Catchment, South China. *Water* **2024**, *16*, 2444. https://doi.org/10.3390/w16172444

Academic Editor: Daniel D. Snow

Received: 8 August 2024
Revised: 25 August 2024
Accepted: 27 August 2024
Published: 29 August 2024

1. Introduction

The chemical weathering of rocks significantly contributes to the hydrogeochemical evolution at the basin scale and plays a crucial role in the global carbon cycle [1,2]. Surface rivers serve as a vital conduit for carbon transport within the Earth's surface system and are essential for investigating the mechanisms of chemical weathering [3]. Chemical weathering of carbonate and silicate rocks is the main contributor to the formation of geological carbon sinks [4,5]. They absorb atmospheric CO_2 during chemical weathering to form bicarbonate, influencing the atmospheric CO_2 balance, and it is a critical issue in global climate change research [6,7]. The carbon sink from carbonate rocks was several times larger than silicate rock, and the chemical weathering of carbonate rocks is a crucial link in the karst processes [2,8]. In the tropical and subtropical regions of southern China,

carbon sequestration in karst areas has a huge potential to increase carbon sinks and is of practical significance in terrestrial carbon sink estimation [9].

For carbonate watersheds, runoff processes are the main controlling factor of weathering intensity [10]. Driven by hydrological processes, major ions resulting from rock weathering engage in the water cycle as river solutes [11], exerting a profound influence on the evolution and the response of the basin's hydrogeochemical features [12,13]. Notably, rivers exhibit considerable variation in the ion's concentration, contingent upon the distinct lithologies involved in chemical weathering [14,15]. In watersheds with different lithology mixtures, the chemical weathering rate of carbonate rocks can be up to 4.4–10.8 times that of silicate rocks [16,17]. With the development of the socio-economic environment, the anthropogenic impact on river water is continuously increasing [18,19]. The ensuing rise in inorganic acid levels within the watershed accelerates the chemical weathering of rocks and diminishes the consumption of atmospheric CO_2, consequently reducing the carbon sink [20–26]. In the presence of nitric acid or sulfuric acid, the dissolved inorganic carbon formed by chemical weathering comes entirely from carbonate rocks, with no consumption of atmospheric CO_2. Therefore, in the process of chemical weathering in a watershed, it is necessary to consider the impact of anthropogenic inputs; otherwise, the chemical weathering rate will be underestimated [27–29].

This paper selects the Qingtang River watershed, a secondary tributary of the Beijiang River in the Pearl River Basin in southern China, as the study area. The watershed features pronounced lithological variations between its upper and lower reaches, coupled with a relatively high anthropogenic intensity. This study employs hydrochemical and isotopic analyses to investigate the origins of hydrochemical ions and their evolutionary traits across various lithologies and levels of anthropogenic intensity, grounded in a comprehensive understanding of the watershed's hydrological cycle. By improving the straightforward model of rock weathering within the watershed, the research quantifies the anthropogenic inputs under conditions of substantial anthropogenic disturbance on the contribution rates of ion sources. Furthermore, the study quantifies changes in chemical weathering rates due to exogenous acid inputs and analyzes the response of chemical weathering to anthropogenic intensity in lithologically mixed catchments.

2. Materials and Methods

The Qingtang River basin, situated in the northern region of Guangdong Province (Figure 1A), is a tributary of the Beijiang River within the Pearl River basin. It originates in Shaoguan City, Guangdong Province, and traverses Huilong Town and Qingtang Town, extending 49 km in length with a drainage basin covering 325 km^2. The area is in the transition zone between the tropical and subtropical regions, with an average annual rainfall of 1859.3 mm and an average evaporation of 946.5 mm [30]. Guangdong Province is among the areas in China most affected by acid rain. In Shaoguan City, the location of our study area, precipitation pH levels fluctuate between 5.0 and 5.6 [31]. The area southwest of Qingtang Town has a higher intensity of human activities (Figure 1C).

The study area mainly consists of a medium to low hilly terrain, with elevations ranging from 72 to 1169 m a.s.l. The terrain gradually decreases in the northwest direction (Figure 1B), and the karst landforms in the middle and lower reaches present a combination of isolated peaks and peak clusters. Forest land is the most extensive, accounting for 72.9%. The arable land is mainly distributed in the Quaternary cover area, accounting for 17.1%, with paddy fields being predominant. The area is silicate rock 44%, carbonate rock 17%, clastic rock 26%, and Quaternary loose sediments 14%. The silicate rock is mainly Middle and Late Jurassic granites, which are formed by quartz, feldspar, and mica. The carbonate rock formations are predominantly thick-bedded limestones of the Lower Carboniferous periods, which are formed by calcite and dolomite. The clastic sequences are chiefly composed of sandstones and shales from the Lower Carboniferous and Upper Devonian periods, which are formed by quartz and clay minerals. The Quaternary sediments consist of sandy clay and sand–gravel layers. The main rock forming minerals are calcite and

quartz, and the natural dissolution equations are: $CaCO_3 + CO_2 + H_2O \rightarrow Ca^{2+} + 2HCO_3^-$, $SiO_2 + 2CO_2 + 2H_2O \rightarrow H_2SiO_3 + 2H_2CO_3$.

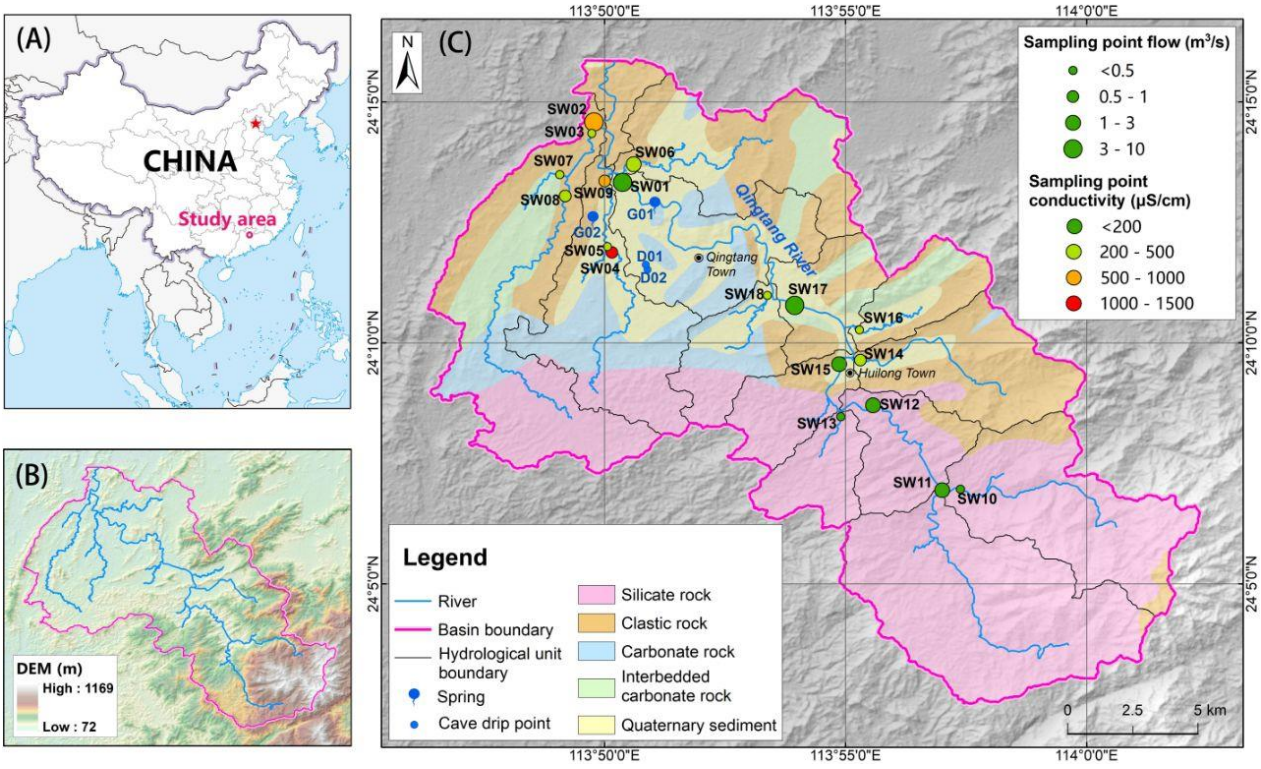

Figure 1. Location of the study area and distribution of sampling points. (**A**) is the location map of study area; (**B**) is the geomorphologic map; (**C**) is geological map with sampling points.

Within the delineated hydrological unit, a network of 18 surface water monitoring points, designated SW01 through SW18, was established. Two karst spring points (G01–G02) and two cave drip points (D01–D02) are located in the isolated peak and peak cluster area in the lower reaches of the watershed (Figure 1C). The G01 spring lies from the thick-bedded limestone strata of the lower Carboniferous and is a typical karst spring with a significant karst conduit. The G02 spring catchment area extends across Quaternary deposits, clastic rock hills, and karst formations. The D01 and D02 drip water points are situated within the caves of the karst peak cluster area.

In June 2023, a field survey was conducted at 18 surface water sample sites (SW01–SW18), 2 karst spring points (G01–G02), and 2 karst cave drip points (D01–D02). Hydrochemical and isotope samples were collected at this time. Considering the basin's lithological diversity, the selection of 2 karst spring sites and 2 karst cave drip sites aimed to accurately capture the hydrogeochemical attributes of carbonate formations. Rainwater samples were collected downstream in Qingtang Town, with 7 rainfall events were recorded in June. Multiple flow measurements were taken at surface water points of SW02, SW06, and SW12.

The water chemistry field testing equipment used was a portable multi-parameter water quality meter (Manta 2^{TM} 4.0, Eureka, CA, USA), measuring parameters such as water temperature, pH, and electrical conductivity (EC) with an accuracy of 0.01 °C, 0.01 pH unit, and 0.1 μS/cm. The ion concentrations of K^+, Na^+, Mg^{2+}, and Ca^{2+} in the samples were determined by ICP-OES (IRIS Intrepid II XSP, Thermo Fisher Scientific, Waltham, MA, USA), while HCO_3^-, Cl^-, SO_4^{2-}, and NO_3^- were measured by ion chromatography (861 Advanced Compact IC Metrohm, Herisau, Switzerland) with 0.01 mg/L precision. The dissolved Si concentrations were determined by the spectrophotometric method. The δ^2H and $\delta^{18}O$ in the water relative to the Vienna Standard Mean Ocean Water (V-SMOW) were measured by a high-precision laser spectrometer (LGR LWIA-24d, Arkansas, CA, USA).

The watershed extent of the Qingtang River as well as the boundaries of the hydrological units were extracted by ArcGIS 10.4. Statistical plots for the analysis of sample test data were produced by OriginPro 2024. Hierarchical cluster analysis (HCA) was applied with Ward's method of clustering and Euclidean distances for the measurement intervals [32].

3. Results

On the basis of the hydrological analysis, the watershed was delineated into 10 tributary hydrological units, sequentially numbered to correspond with the sampling points at each tributary. A detailed overview of each unit's characteristics is presented in Table 1. The predominant lithology of each hydrological unit was ascertained with the understanding that the downstream areas, largely covered by Quaternary sediments, were underlain by carbonate formations. In the upper reaches of the watershed, silicate rock predominated, the middle reaches displayed a mixed lithological composition, and the lower reaches were characterized primarily by carbonate rocks.

Table 1. Hydrological unit characteristics in the basin.

Unit Number	Location	Area (km^2)	Basement Rock
SW10	Upper basin	34	Silicate rock
SW11	Upper basin	51	Silicate rock
SW13	Upper basin	11	Silicate rock
SW14	Middle basin	23	Clastic rock
SW15	Middle basin	12	Silicate rock
SW16	Middle basin	11	Clastic rock
SW18	Middle basin	13	Carbonate rock
SW06	Lower basin	29	Carbonate rock
SW09	Lower basin	31	Carbonate rock
SW03	Lower basin	47	Carbonate rock

The main physicochemical parameters of surface water and groundwater in the basin are shown in Table 2. The water temperature at each surface water location showed significant variation, with values between 23.29 °C and 28.74 °C, and a median value of 25.01 °C. The water temperature of the cave drip was significantly lower than that of others. The pH value of surface water ranged from 6.44 to 8.05, with a median value of 7.30. The pH value of cave drip water was higher than that of groundwater. Surface water electronic conductivity (EC) lay between 39.9 and 1262.0 µS/cm, with a median value of 275.7 µS/cm, and the high value was contributed by the hydrological unit where SW04 is located. As shown in Figure 1, EC showed a gradual increasing trend from the upstream granite zone to the downstream karst zone. The EC of karst spring G01 in the karst area was significantly higher than that of G02 in the lithological mixed watershed, and the EC of karst cave drip D01 was significantly smaller than that of D02 due to the difference in water–rock interactions resulting from different runoff paths in the karst vadose zone. The cations in each surface water point were dominated by Ca^{2+} and Na^{+}, and the anions were primarily HCO_3^{-} and SO_4^{2-}. As shown in Figure 2, there were 2 to 3 statistical outliers for each ion, except for HCO_3^{-} and dissolved Si, showing the influence of anthropogenic inputs. Ca^{2+} ranged from 0.106 to 5.017 mmol/L, with a median value of 1.022 mmol/L. Na^{+} ranged from 0.079 to 3.220 mmol/L, with a median value of 0.176 mmol/L. HCO_3^{-} ranged from 0.181 to 3.764 mmol/L, with a median value of 2.078 mmol/L. SO_4^{2-} ranged from 0.044 to 3.417 mmol/L, with a median value of 0.224 mmol/L. The dissolved Si concentration was generally high, ranging from 0.139 to 0.326 mmol/L, with a median value of 0.251 mmol/L, and was a major contributing factor in the upper part of the basin for the contribution of the large silicate rock distribution area. Both springs and cave drips showed typical karst water characteristics, with significantly high Ca^{2+} and HCO_3^{-} contents. SO_4^{2-} and NO_3^{-} associated with anthropogenic emissions were detected in the collected rainwater samples.

The results of deuterium-oxygen isotopes are illustrated in Figure 3. The δ^2H values in surface water ranged from −38.52‰ to −24.99‰, while the $\delta^{18}O$ values ranged from −6.59‰ to −4.55‰. In rainwater, the δ^2H values ranged from −28.05‰ to 0.24‰, and the

$\delta^{18}O$ values ranged from −4.92‰ to −1.92‰. The isotope ranges of groundwater and cave drip water for both $\delta^{2}H$ and $\delta^{18}O$ lay between those of surface water and rainwater.

Table 2. The physicochemical parameters of water samples in study area.

Parameters	Surface Water (*n* = 18)				Groundwater		Cave Drip Water		Rainwater
	Min	Max	Median	S.D.	G01	G02	D01	D02	RW
Temperature (°C)	23.29	28.74	25.01	1.55	23.88	22.24	21.22	21.15	Untested
pH	6.44	8.05	7.30	0.38	6.82	7.29	8.03	7.66	Untested
EC (μS/cm)	39.9	1262.0	275.7	302.1	449.9	296.3	350.6	580.8	Untested
K^+ (mmol/L)	0.042	0.506	0.111	0.110	0.134	0.007	0.004	0.003	0.002
Na^+ (mmol/L)	0.079	3.220	0.176	0.734	0.247	0.003	0.019	0.010	N.D.
Ca^{2+} (mmol/L)	0.106	5.017	1.022	1.226	1.889	0.979	1.947	2.508	0.085
Mg^{2+} (mmol/L)	0.016	0.768	0.173	0.194	0.437	0.098	0.080	0.372	0.001
Cl^- (mmol/L)	0.030	0.774	0.160	0.189	0.282	0.014	0.020	0.015	0.009
SO_4^{2-} (mmol/L)	0.044	3.417	0.224	0.867	0.498	0.172	0.150	0.144	0.028
HCO_3^- (mmol/L)	0.181	3.764	2.078	1.175	3.915	1.777	3.644	5.571	0.241
NO_3^- (mmol/L)	N.D.	2.405	0.003	0.556	0.001	0.014	0.100	0.049	0.019
Si (mmol/L)	0.139	0.326	0.251	0.059	0.192	0.146	N.D.	N.D.	N.D.

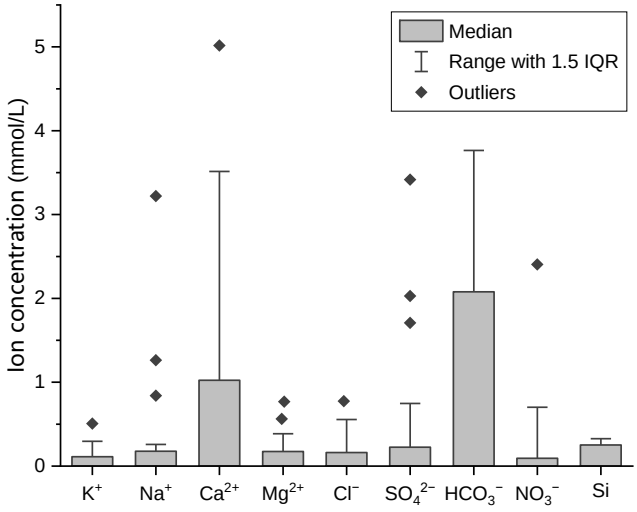

Figure 2. Bar chart and outliers of main ion concentrations in surface water.

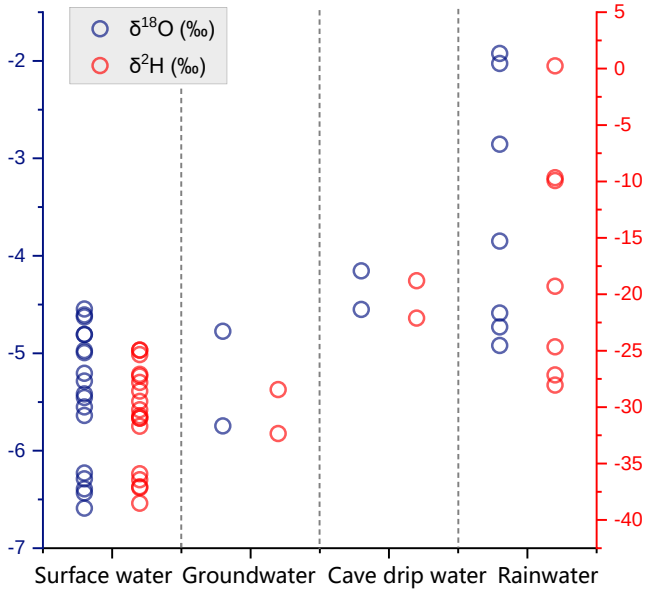

Figure 3. Isotope scatter plot of $\delta^{2}H$ and $\delta^{18}O$.

4. Discussion

4.1. Impact of Lithological Differences on Water Cycle Processes

Isotope scatter plots of different water bodies in the basin were created based on δ^2H and $\delta^{18}O$ isotope results (Figure 4). The local meteoric water line (LMWL: $\delta^2H = 7.82 \times \delta^{18}O + 7.84$) was fitted by rainwater samples, and the points was located above the global meteoric water line (GMWL: $\delta^2H = 8 \times \delta^{18}O + 10$). The surface water evaporation line (EL: $\delta^2H = 6.36 \times \delta^{18}O + 3.75$) was closer to the LMWL, suggesting a relatively swift cycle renewal rate. A distinct zoning pattern was observed in Figure 4 for the upstream and downstream regions of the basin. The upstream area, dominated by silicate rocks, generally displayed more negative isotope values, whereas the downstream area, characterized by carbonate rocks and cave drip waters, aligned more closely with recent rainwater isotope values, indicating that the runoff processes in the downstream karst area were faster by the influence of recent precipitation. The outlet of the watershed (SW02) was situated at the transition between the upstream silicate rock hydrological unit and the downstream carbonate rock hydrological (Figure 4), signifying a confluence of two runoff types with distinct circulation properties. The surface water sampling points were all located in the lower left of the intersection of the EL and the LMWL, suggesting that the general circulation rate of surface water in this watershed is relatively fast, and the surface water isotopes did not show the evaporation fractionation characteristics induced by long-term retention. Groundwater sampling points were arrayed between rainwater and surface water signatures and were proximate to the LMWL, suggesting that, in terms of regional recharge sources and deep groundwater circulation, there was no evidence of extensive long-distance or deep groundwater recharge [33]. Cave drip water points were positioned in the upper right relative to both surface and groundwater, with isotopic signatures akin to rainwater, denoting that the vertical percolation of precipitation through the karst vadose zone was the immediate source for the cave drip waters.

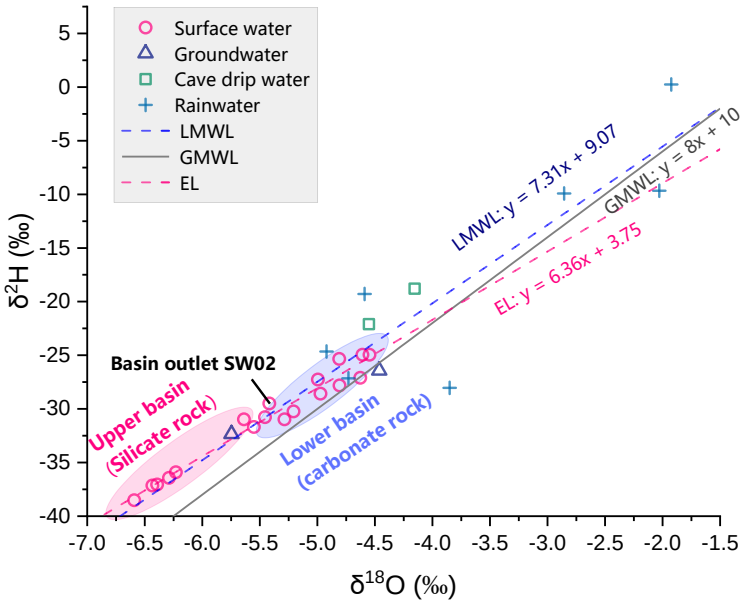

Figure 4. Isotope scatter plots of δ^2H and $\delta^{18}O$ for different lithologic conditions.

4.2. Control of Hydrogeochemical Processes by Lithological Differences

On the basis of the ion concentrations results, a Piper diagram (Figure 5) was constructed [34]. Surface water, groundwater, and cave drip water are gathered in the light blue area on the left side, corresponding to the hydrological units within the carbonate rock distribution zone of the mid-lower reaches, indicating that there was a certain degree of interaction between surface water and karst groundwater [35], reflecting that karst processes were the primary controllers of hydrogeochemical processes, consistent with

related studies in the Lijiang River basin [36]. Units from the upstream silicate rock were denoted in the red area on the right side of the diagram. In contrast to the carbonate rock units, a significant rise in the Na^+ concentration was observed, indicating the primary impact of granite over limestone on the hydrochemical composition of the basin. Additionally, along the runoff path, there was a significant rise in the proportions of Cl^-, NO_3^-, and SO_4^{2-} ions, as indicated by the red arrows in Figure 5, indicative of a leaching effect. For the hydrological unit at SW04, located downstream, ion concentrations were markedly higher than in other units due to industrial influences. As surface water and groundwater continuously converge along the runoff pathway, the river's hydrochemical components exhibited a notable dilution effect, signified by the green arrow in Figure 5. Similar dilution phenomena were reported occurring in scenarios characterized by upstream anthropogenic inputs and the confluence of surface and subsurface runoff as the river flowed downstream [37]. Influenced by the mixing of runoff, the hydrochemical evolution of this anthropogenically impacted unit trends towards the blue area indicative of the carbonate rock zone (Figure 5). The concentration of Na^+ was the highest at the outlet (SW02), which was speculated to be affected by the high intensity of anthropogenic discharges and the water regulation of downstream reservoirs.

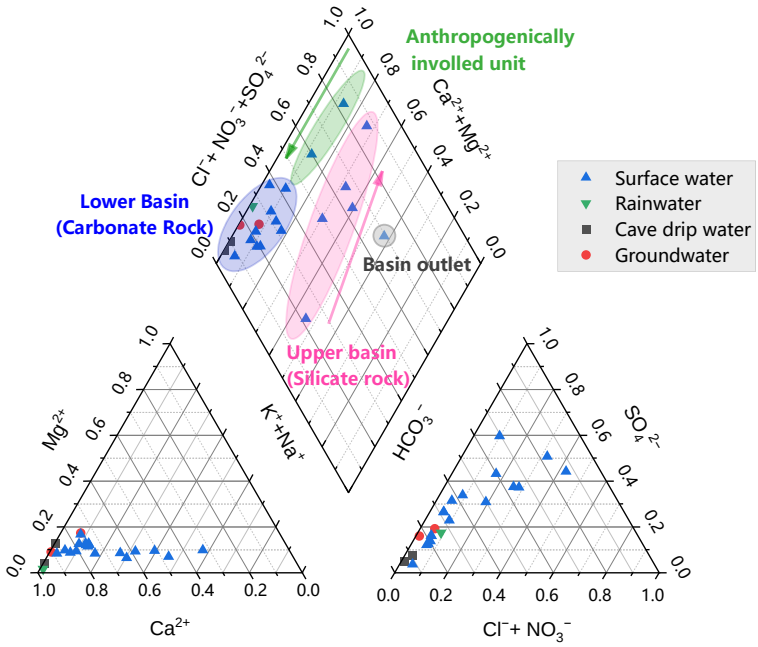

Figure 5. Piper diagram and main hydrogeochemical processes.

The molar concentration ratios of ions in river water could reveal the intensity of chemical weathering, and employing these ratios could elucidate the origins of hydrochemical components across various hydrological units [26,38–41]. The analysis of molar concentration ratios is depicted in Figure 6A,B, demonstrating significant zonation between the upstream silicate rock region and the downstream carbonate rock region. Samples from the upstream aligned closely with the endmembers of silicate rocks, while those from the downstream approximated the end-members of carbonate rocks. The hydrochemical ions in different hydrological units were predominantly governed by the weathering of the respective stratigraphic rocks. At the watershed's outlet, the water chemistry of SW02 reflected characteristics akin to an evaporite end-member, influenced by a substantial Na^+ influx anthropogenically. Consequently, the water chemistry of the hydrological units in the Qingtang River basin was primarily shaped by the chemical weathering of rocks of different lithologies, with certain areas subject to anthropogenic impacts. In addition to the direct anthropogenic inputs of sulfate and nitrate, the chemical weathering of carbonate rocks, facilitated by the action of sulfuric and nitric acids, could also yield NO_3^- and SO_4^{2-} [1]. In Figure 6C, there was a linear positive correlation between [Ca^{2+} + Mg^{2+}] and [NO_3^-

+ SO_4^{2-}], suggesting that the influence of exogenous acids on chemical weathering was prevalent in the watershed, and that sulfate and nitrate were significant contributors to the role of anthropogenic interventions in the watershed's hydrochemistry characteristics. In Figure 6C, a linear positive correlation existed between [Ca^{2+} + Mg^{2+}] and [NO_3^- + SO_4^{2-}], indicating that the influence of exogenous acids, represented by sulfuric and nitric acids, was pervasive within the watershed. Sulfates and nitrates served as significant indicators of anthropogenic intervention in the hydrochemical characteristics of the basin.

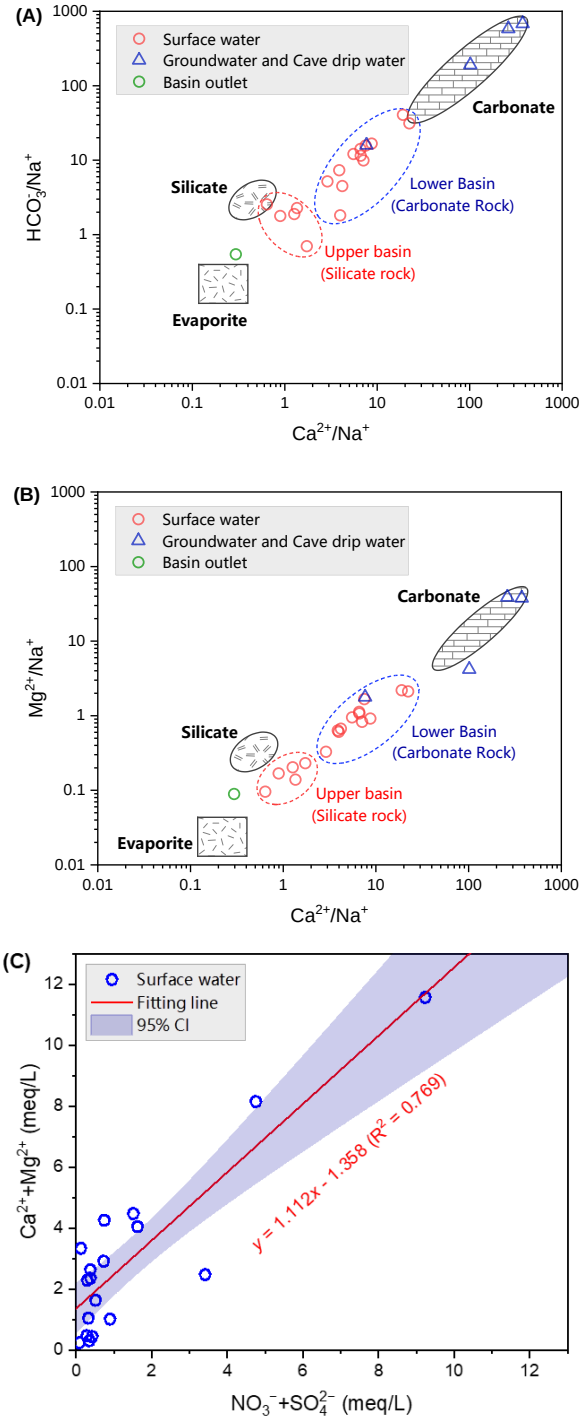

Figure 6. Scatter plot of molar concentration ratios. (**A**) Co-variation in (HCO_3^-/Na^+) and (Ca^{2+}/Na^+); (**B**) co-variation in (Mg^{2+}/Na^+) and (Ca^{2+}/Na^+); and (**C**) equivalent ratios of [Ca^{2+} + Mg^{2+}] and [NO_3^- + SO_4^{2-}].

4.3. Impact of Anthropogenic Activities on Hydrochemistry Characteristics

In order to define the extent of anthropogenic impacts on the hydrochemical components of different hydrological units, HCA was employed in the analysis. The method groups samples on the basis of the degree of similarity of multiple hydrochemical parameters from different samples, demonstrating homogeneity within groups and heterogeneity between groups. It is a well-established method for examining the relationships and distribution patterns within hydrogeochemical datasets [42–45]. The outcomes of the HCA are depicted in Figure 7. A Euclidean distance threshold of 15 was utilized to segregate the samples into three distinct clusters, labeled C1, C2, and C3, with samples within the same cluster denoted by identical symbols in the figure. Cluster C1 predominantly mirrored the hydrogeochemical processes and mixing dynamics within the silicate rock regions, encompassing samples SW01, SW10, SW11, SW12, SW13, SW15, and SW17. SW01 and SW17 were situated in the downstream and midstream regions of the carbonate rock distribution area, respectively. Their positioning led to mixing with surface water from the upstream silicate rock area, which in turn imparted certain characteristics of the silicate rock surface water to their chemical profiles. Cluster C2 predominantly represented the hydrogeochemical processes and the effects of mixing occurring within the downstream carbonate rock watersheds. This cluster encompassed samples SW03, SW06, SW07, SW08, SW14, SW16, and SW18. The samples in C1 and C2 showed significant correlation between stratigraphic lithology and spatial distribution of hydrological units. C3 was the mixing of anthropogenic impacts and hydrogeochemical processes in the watershed, and contained samples SW02, SW04, and SW09. Notably, SW04 and SW09 were situated within the same hydrological unit. SW02 represented the confluence of the tributary with the main river flow within this hydrological unit. The principal outlier ions for C3 were highlighted by elevated concentrations: Na^+ in SW02 at 3.220 mmol/L, accompanied by SO_4^{2-} at 1.707 mmol/L; SW04 exhibited Na^+ at 1.263 mmol/L, SO_4^{2-} of 3.417 mmol/L, and additionally high NO_3^- levels at 2.405 mmol/L; and SW09 showed Na^+ at 0.839 mmol/L and SO_4^{2-} at 2.028 mmol/L.

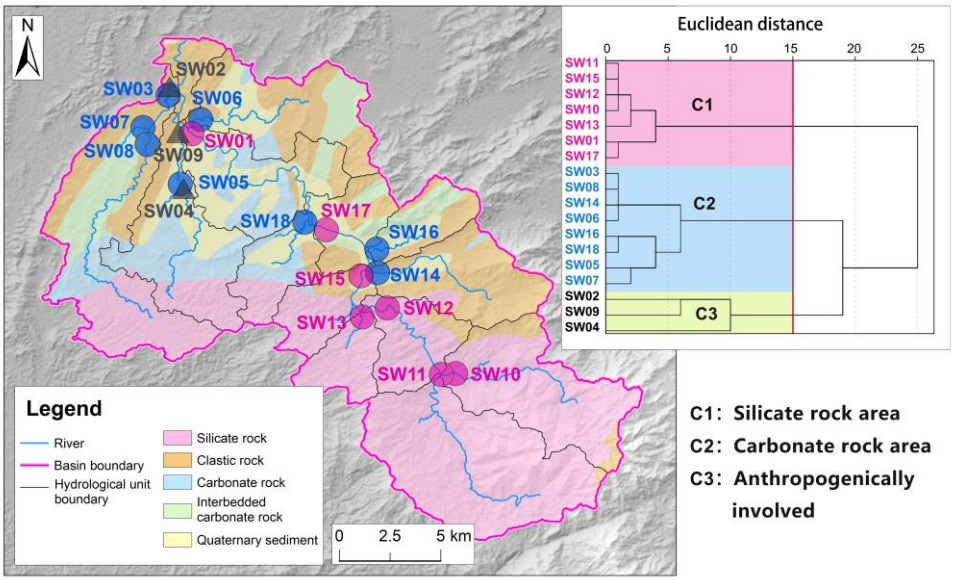

Figure 7. Spatial distribution of hierarchical cluster analysis.

Within the three clusters, C1 and C2 predominantly mirrored the hydrogeochemical processes in their natural state, while C3 represented the chemical weathering processes of carbonate rocks under strong anthropogenic interference. Therefore, when anthropogenic interference reached a certain intensity, it could dominate the hydrogeochemical processes of the hydrological unit and even the mainstream hydrochemistry, leading to the special characteristics of hydrogeochemical responses in the watershed.

The Gibbs diagram is frequently utilized to delineate the progression of hydrogeochemical processes, encompassing rock weathering (water–rock interactions), precipitation, and evaporation [46,47]. As depicted in Figure 8, the plot clearly delineated the zoning of surface waters within clusters C1, C2, and C3. Cluster C1, situated in the silicate rock region, indicated a low total dissolved solids (TDS) condition, primarily influenced by dilution from atmospheric precipitation, with samples positioned near the precipitation zone in the lower right section of the diagram. Groundwater and cave drip water samples were arrayed on the mid-left side, predominantly shaped by water–rock interactions with carbonate rocks, exhibiting high concentrations of Ca^{2+} and HCO_3^-. Surface water samples of Cluster C2, akin to groundwater, signified the chemical weathering of carbonate rocks. Conversely, Cluster C3 surface waters, which were influenced by significant human inputs, exhibited an abnormal increase in Na^+, K^+, SO_4^{2-}, and NO_3^-, reflecting a high TDS state, with a sample distribution inclined towards the upper right corner of the diagram.

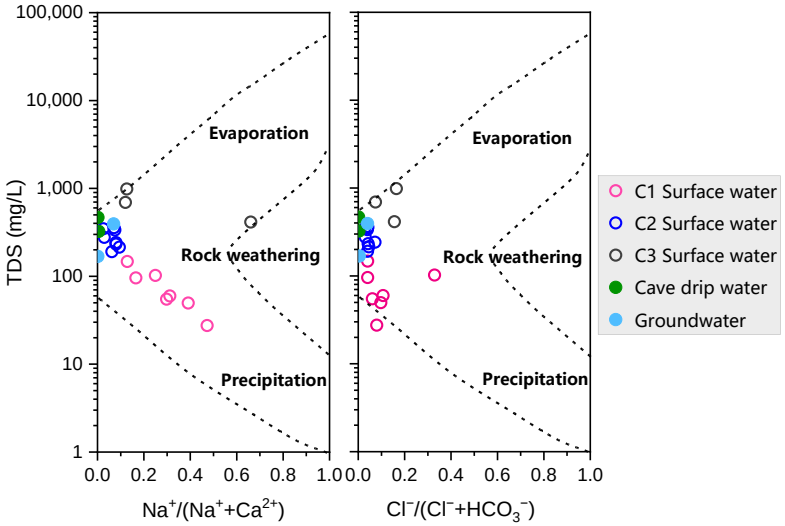

Figure 8. Gibbs diagrams for samples in study area.

4.4. Limitations of the Straightforward Method for Calculating the Contribution Ratio of Major Cations

The flux of an element *X* can be expressed by Equation (1) by use of the straightforward method on the basis of the main sources of solute in surface water (atmospheric inputs, rock weathering, and anthropogenic inputs) [48]:

$$[X]_{water} = [X]_{atmospheric} + [X]_{anthropogenic} + [X]_{carbonate} + [X]_{silicate} \quad (1)$$

where $[X]_{water}$ denotes the concentration of ions expressed in mmol/L, $[X]_{atmospheric}$ represents the flux of atmospheric inputs, $[X]_{anthropogenic}$ represents the flux of anthropogenic inputs, $[X]_{carbonate}$ represents the flux of carbonate weathering, and $[X]_{silicate}$ signifies the flux of silicate weathering.

The following assumptions must be met in the calculation process: (1) the Cl^- present in river water is entirely sourced from atmospheric and anthropogenic input; (2) the input of Na+ from human activities is in equilibrium with Cl^-, after accounting for atmospheric inputs; (3) there is no anthropogenic input of K^+, Ca^{2+}, and Mg^{2+}; and (4) the presence of Ca^{2+} and Mg^{2+} in surface water is exclusively the result of carbonate rock dissolution.

For the estimation of the atmospheric input, Cl^- can be properly corrected by use of the P/R method due to its conservative geochemical properties, where P and R represent the atmospheric precipitation and runoff in the region, respectively [38,49,50]. The average rainfall and evaporation in the area are 1895.3 mm and 946.5 mm, respectively. The cations

from other atmospheric inputs are determined on the basis of their molar ratio relative to Cl^- in the rainwater. Accordingly, Equation (1) can be decomposed into the subsequent equations:

$$[Cl^-]_{atmospheric} = [Cl^-]_{rainwater} \times (P/R) = 0.0186 \text{ mmol/L} \quad (2)$$

$$[Cl^-]_{water} = [Cl^-]_{atmospheric} + [Cl^-]_{anthropogenic} \quad (3)$$

$$[Cl^-]_{anthropogenic} = [Na^+]_{anthropogenic} \quad (4)$$

$$[Na^+]_{water} = [Na^+]_{atmospheric} + [Na^+]_{anthropogenic} + [Na^+]_{silicate} \quad (5)$$

$$[K^+]_{water} = [K^+]_{atmospheric} + [K^+]_{silicate} \quad (6)$$

$$\left[Mg^{2+}\right]_{water} = \left[Mg^{2+}\right]_{atmospheric} + \left[Mg^{2+}\right]_{carbonate} + \left[Mg^{2+}\right]_{silicate} \quad (7)$$

$$\left[Ca^{2+}\right]_{water} = \left[Ca^{2+}\right]_{atmospheric} + \left[Ca^{2+}\right]_{carbonate} + \left[Ca^{2+}\right]_{silicate}. \quad (8)$$

In the context of watersheds experiencing substantial anthropogenic disturbances, the aforementioned assumptions may not hold true. The straightforward method struggles to accurately discern the contribution rate of human-induced alterations. The detection of anomalous ion concentrations in surface water C3 suggests the presence of anthropogenic inputs of Na^+ and K^+. Consequently, there is a necessity to refine the calculation methodology to effectively assess the contribution rate of anthropogenic influences.

4.5. Calculation of Cation Contribution Ratio under Anthropogenic Interference

In the case of significant anthropogenic disturbance, the influx of Na^+ and K^+ ions in the form of sulfates and nitrates, which are anthropogenic in origin, will be mischaracterized by the straightforward method as contributions from silicate rock weathering. Therefore, in order to identify this portion of Na^+ and K^+, Equations (4)–(6) can be replaced by Equation (9):

$$[Na^+]_{water} + [K^+]_{water} = [Na^+]_{atmospheric} + [K^+]_{atmospheric} + [Cl^-]_{anthropogenic} + [NO_3^-]_{anthropogenic} + \left[SO_4^{2-}\right]_{anthropogenic} + [Na^+]_{silicate} + [K^+]_{silicate}. \quad (9)$$

In Equation (9), the concentrations of Na^+ and K^+ ions derived from the weathering of silicate rocks can be ascertained through the concentrations of dissolved Si in the water. The chemical weathering reactions occurring within the silicate rock watershed are delineated in Equations (10) and (11). Near the study area, the ratios of silicate rock minerals are known: (Ca + Mg)/(K + Na) equals 0.139, K/Na equals 1.253, Ca/Na equals 0.212, and Mg/Na equals 0.099 [51]. With these ratios, we can determine the amounts of Ca^{2+}, Mg^{2+}, K^+, and Na^+ ions produced by silicate rock weathering.

$$Na_xK_{1-x}AlSi_3O_8 + CO_2 + 6H_2O \rightarrow xNa^+ + (1-x)K^+ + HCO_3^- + 3H_4SiO_4 + Al(OH)_3 \quad (10)$$

$$Ca_xMg_{1-x}Al_2Si_2O_8 + 2CO_2 + 8H_2O \rightarrow xCa^{2+} + (1-x)Mg^{2+} + 2HCO_3^- + 2H_4SiO_4 + 2Al(OH)_3. \quad (11)$$

Equations (2), (3), and (7)–(11) were applied to calculate the respective ion sources and contributions in the samples, with the outcomes depicted in Figure 9. In general, atmospheric inputs averaged a contribution of 17.65%, anthropogenic inputs 21.05%, carbonate rock weathering 51.77%, and silicate rock weathering 9.54%. The average contribution of atmospheric constituents is 33.08% for C1, 9.57% for C2, and 3.19% for C3. The contribution of atmospheric input in C1 with lower TDS was significantly higher than that in C2 and C3 with higher TDS. This result is consistent with the trend of the hydrochemical evolution of surface water in C1 in Figure 8, which was significantly biased toward the end-member of precipitation, indicating that atmospheric input was a significant contributor to the

hydrochemistry in silicate rock watersheds with lower TDS. The average contribution of silicate rock weathering in C1 was 19.29% and that of carbonate rock weathering in C2 was 74.68%, demonstrating the difference in the effect of chemical weathering on the water chemistry of different lithologies during natural conditions [35]. The highest contribution of anthropogenic input was SW02 in C3 with 71.23% and the lowest was SW16 in C2 with only 3.85%. The contribution of anthropogenic input was relatively easier to highlight by the low TDS in the silicate rock zone. If the presence of Na^+ in the form of sulfate in SW02 was ignored, the contribution of anthropogenic inputs was calculated to be only 11.09%. The excess Na^+ would result in an elevated contribution of 80.31% to weathering of silicate rocks, which was clearly inconsistent with the actual conditions. Therefore, for conditions where Na^+ and K^+ inputs in the form of sulfate and nitrate were significant in watersheds, the methodology presented in this paper offered an effective approach to accurately quantify the contributions from anthropogenic inputs.

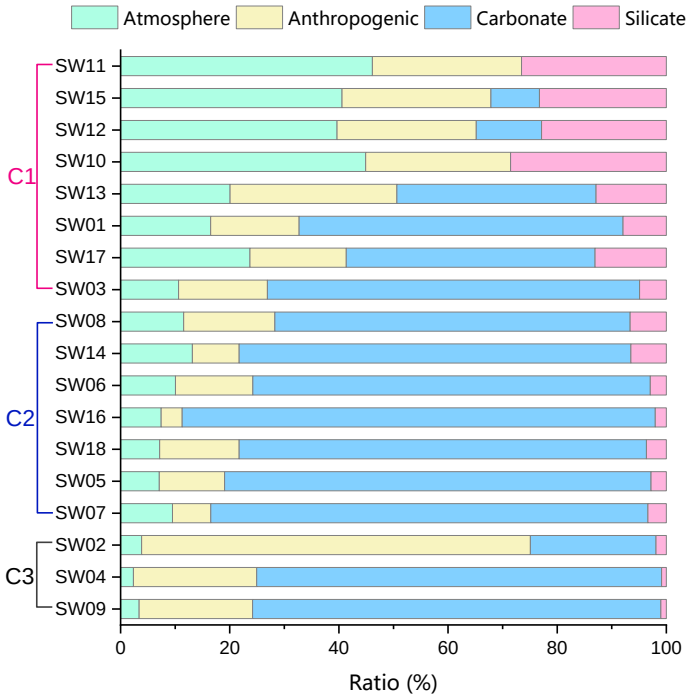

Figure 9. Contributions of four sources to the total cation concentrations in surface water.

In the prevalent scenario of watersheds subjected to cationic interference, which is becoming increasingly common in high anthropogenic intensity, the anthropogenic influx of ions extends beyond the conventional NaCl form to include the nitrate and sulfate salts of Na^+ and K^+. In such cases, how can the contribution of chemical weathering be calculated by simple water chemistry and ion calculations? It is necessary to conduct field hydrogeological surveys to clarify the hydrochemical characteristics and primary sources, identify specific ionic interferences, and then apply the methodology presented in this paper for calculations.

4.6. Anthropogenic Involved Chemical Weathering Rates

In addition to the anthropogenic input of Na^+ and K^+, for watersheds with high anthropogenic intensity, exogenous acids, mainly sulfuric and nitric acids, can directly affect the weathering processes of carbonate rocks, with the Equations (12) and (13):

$$2Ca_xMg_{1-x}CO_3 + H_2SO_4 \rightarrow 2xCa^{2+} + 2(1-x)Mg^{2+} + 2HCO_3^- + SO_4^{2-} \quad (12)$$

$$Ca_xMg_{1-x}CO_3 + HNO_3 \rightarrow xCa^{2+} + (1-x)Mg^{2+} + HCO_3^- + NO_3^-. \quad (13)$$

Exogenous acids are recognized for their capacity to expedite the weathering of carbonates [29]. In order to identify the impact of anthropogenic discharges on the source of HCO_3^-, it is imperative to segregate and calculate the HCO_3^- generated from carbonic acid, silicic acid, and exogenous acid reactions individually. Weathering of carbonate rocks by different acids is in accordance with Equation (19):

$$\left[HCO_3^-\right]_{water} = \left[HCO_3^-\right]_{carbonic} + \left[HCO_3^-\right]_{silicic} + \left[HCO_3^-\right]_{exogenous} \quad (14)$$

where $\left[HCO_3^-\right]_{carbonic}$ denotes the HCO_3^- resulting from the weathering of carbonates by carbonic acid, $\left[HCO_3^-\right]_{silicic}$ signifies the HCO_3^- produced by the weathering of carbonates via silicic acid, and $\left[HCO_3^-\right]_{exogenous}$ signifies the HCO_3^- produced by the weathering of carbonates via exogenous acid.

In scenarios where exogenous acids are present and there is an absence of Ca^{2+} and Mg^{2+} from anthropogenic inputs, the subsequent Equations (15)–(17) become applicable.

$$\left[Ca^{2+}\right]_{water} + \left[Mg^{2+}\right]_{water} = \left[Ca^{2+}\right]_{carbonic} + \left[Mg^{2+}\right]_{carbonic} + \left[Ca^{2+}\right]_{silicic} + \left[Mg^{2+}\right]_{silicic} + \left[Ca^{2+}\right]_{exogenous} + \left[Mg^{2+}\right]_{exogenous} \quad (15)$$

$$\left[HCO_3^-\right]_{exogenous} = \left[Ca^{2+}\right]_{exogenous} + \left[Mg^{2+}\right]_{exogenous} \quad (16)$$

$$\left[HCO_3^-\right]_{carbonic} = 2 \times \left(\left[Ca^{2+}\right]_{carbonic} + \left[Mg^{2+}\right]_{carbonic}\right). \quad (17)$$

Utilizing Equations (10) and (11) in conjunction with the molar ratio (Ca + Mg)/(K + Na) = 0.139 specific to silicate rocks, we can determine the quantities of HCO_3^- and the combined calcium and magnesium ions (Ca^{2+} + Mg^{2+}) resulting from the weathering of carbonate rocks by silicic acid, as shown in Equations (18) and (19).

$$\left[HCO_3^-\right]_{silicic} = (2 \times 0.139 + 1)/(2 \times 0.139 + 3) \times [Si] \quad (18)$$

$$\left[Ca^{2+}\right]_{silicic} + \left[Mg^{2+}\right]_{silicic} = 0.139/(2 \times 0.139 + 3) \times [Si] \quad (19)$$

The chemical weathering rate (CWR) for both silicate and carbonate rocks is derived from the mass concentrations of their respective ions, as delineated in Equations (20) and (21):

$$[CWR]_{silicate} = \left(\left[Na^+\right]_{silicate} + \left[K^+\right]_{silicate} + \left[Ca^{2+}\right]_{silicate} + \left[Mg^{2+}\right]_{silicate} + [Si]\right) \times Q/S \quad (20)$$

$$[CWR]_{carbonate} = \left(\left[Ca^{2+}\right]_{carbonate} + \left[Mg^{2+}\right]_{carbonate} + 0.5 \times \left[HCO_3^-\right]_{carbonate} + \left[Ca^{2+}\right]_{exogenous} + \left[Mg^{2+}\right]_{exogenous} + \left[HCO_3^-\right]_{exogenous}\right) \times Q/S \quad (21)$$

where Q is the total annual runoff and S is the catchment area, the calculation results are shown in Table 3.

Table 3. Anthropogenically involved chemical weathering rates.

Sample	Annual Runoff ($10^7 m^3 \cdot a^{-1}$)	Watershed Area (km^2)	CWR_Silicate ($t \cdot km^{-2} \cdot a^{-1}$)	CWR_Carboncate ($t \cdot km^{-2} \cdot a^{-1}$)	CWR_Carboncate without Exogenous Acids ($t \cdot km^{-2} \cdot a^{-1}$)
SW02	18.0	325	9.9	62.4	48.8
SW06	1.6	29	5.8	75.4	62.0
SW12	5.9	85	14.5	7.3	4.3

The chemical weathering rate of carbonate rocks in the Qingtang River basin, influenced by exogenous acids, was calculated to be 62.4 $t \cdot km^{-2} \cdot a^{-1}$, according to the

sample SW02 obtained at the watershed's outlet. Excluding the effect of exogenous acids in these calculations would yield a weathering rate of 48.8 $t \cdot km^{-2} \cdot a^{-1}$. The presence of exogenous acids in the chemical weathering of carbonate rocks resulted in an actual weathering rate that was 27.87% higher, reflecting a notable enhancement attributable to anthropogenic influences. In the downstream carbonate basin, the weathering rate at site SW06 is 75.4 $t \cdot km^{-2} \cdot a^{-1}$, which closely aligns with the calculated rate of 75.1 $t \cdot km^{-2} \cdot a^{-1}$ observed in the Pearl River basin [16]. In contrast, the silicate rock weathering rate at site SW12 is 14.5 $t \cdot km^{-2} \cdot a^{-1}$, a value that is lower than the 20.7 $t \cdot km^{-2} \cdot a^{-1}$ recorded at Shijiao Station, another location within the Beijiang River basin of the Pearl River system [16].

The disparity in chemical weathering rate among various lithologies was pronounced. In southern China, watersheds commonly exhibit a combination of carbonate and silicate rocks, a geologic trait that significantly influences the local hydrogeochemical cycles. Chemical weathering, particularly within carbonate basins, is frequently exacerbated by the presence of sulfuric and nitric acids, a phenomenon that is well-documented in the literature [29,52,53]. The variability in the anthropogenically influenced chemical weathering rates observed in the Qingtang River basin is considered to be regionally indicative, reflecting the broader hydrogeochemical responses to human activities in the area.

5. Conclusions

The research area is located in a watershed where the upstream region is primarily composed of silicate rocks, while the downstream region is dominated by carbonate rocks with a mixture of minor clastic rocks. Broadly speaking, the hydrogeochemical processes are mainly controlled by the weathering of the underlying rock strata, with some local hydrologic units significantly influenced by anthropogenic inputs. Stable isotopes of deuterium and oxygen suggest that the watershed experiences a relatively rapid rate of water cycling, with runoff in the downstream carbonate areas exhibiting a marginally quicker pace compared to the upstream silicate regions. The TDS are typically observed to be lower in the upstream areas as opposed to the downstream zones, indicative of a filtration process occurring as the river flows. Hydrological units significantly impacted by human-induced discharges demonstrate a dilution effect along the river's trajectory. The effect of precipitation on the water chemistry of the watershed is particularly significant in the low TDS silicate rock zone. The type of chemical weathering deduced from the ratios of chemical ions in the water aligns with the distribution of rock types in both the upstream and downstream areas. This concordance substantiates the notion that rock weathering exerts a decisive influence on the hydrochemical composition within each hydrological unit.

Human activities affect the watershed mainly in two aspects: (1) the direct input of ions alters the hydrogeochemical processes of different hydrological units, and (2) the input of exogenous acids accelerates the chemical weathering of rocks within the watershed. When there is anthropogenic input of Na^+ and K^+ beyond the original hypothetical conditions, the calculation method for the source and contribution rate of the straightforward model will incorrectly account for some of the human-introduced ions as chemical weathering of silicate rocks, thereby reducing the contribution rate of anthropogenic inputs. The methodology presented in this paper takes into account the diverse origins of Na^+ and K^+, accurately assessing the contribution of human activities. The calculated results reveal the following: the average contribution rate of atmospheric input is 17.65%, exerting a substantial influence on the formation of cations in silicate rock watersheds; the average contribution of anthropogenic inputs stands at 21.05%, peaking at 71.08%, becoming the principal factor controlling the hydrogeochemical processes in some specific hydrological units; and the average contribution from carbonate rock weathering is 51.77%, whereas silicate rock contributes 9.54%. A marked disparity exists in the weathering rates between carbonate and silicate rocks. In watersheds with mixed lithologies, a higher proportion of carbonate can produce a higher rate of rock weathering. The input of exogenous acids elevates the weathering rate of carbonate rocks in the watershed to 62.4 $t \cdot km^{-2} \cdot a^{-1}$,

marking a 27.87% enhancement over the weathering rate calculated without considering the role of exogenous acids.

Author Contributions: F.L.: conceptualization, formal analysis, investigation, data curation, software, writing—original draft, writing—review and editing; S.W.: methodology, investigation; J.W.: formal analysis, resources; F.G.: conceptualization, resources; S.Y. and P.S.: resources, validation. All authors have read and agreed to the published version of the manuscript.

Funding: This work was supported by the Guangxi Natural Science Foundation (2023GXNSFBA026254), Scientific research capacity building project for Guilin Karst Geology Observation and Research Station of Guangxi (GUIKE 23-026-274), the Institute of Karst Geology Fundamental Research Project (2023012), Project of geological exploration and urban geology in Guangdong Province (2023-30), Scientific research project of Guangdong Hydrogeological Battalion (YRSF2024168), the National Natural Science Foundation of China (42302296) and the China Geological Survey (DD20230547).

Data Availability Statement: The data presented in this study are available on request from the corresponding authors.

Acknowledgments: Our special thanks are given to Guanghui Jiang whose invaluable comments greatly improved the manuscript, and Zhenzhao Zhou, Tao Hou and Weiqiang Song for their help with field work.

Conflicts of Interest: The authors declare no conflicts of interest.

References

1. Martin, J. Carbonate minerals in the global carbon cycle. *Chem. Geol.* **2017**, *449*, 58–72. [CrossRef]
2. Liu, Z.; Macpherson, G.L.; Groves, C.; Martin, J.B.; Yuan, D.; Zeng, S. Large and active CO_2 uptake by coupled carbonate weathering. *Earth Sci. Rev.* **2018**, *182*, 42–49. [CrossRef]
3. Li, S.; Liu, L.; Suo, Y.; Li, X.; Zhou, J.; Jiang, Z.; Guan, H.; Sun, G.; Yu, L.; Liu, P.; et al. Carbon Tectonics: A new paradigm for Earth system science. *Chin. Sci. Bull.* **2023**, *68*, 309–338. [CrossRef]
4. Tao, Z.; Gao, Q.; Wang, Z.; Zhang, S.; Xie, C.; Lin, P.; Ruan, X.; Li, S.; Mao, H. Estimation of carbon sinks in chemical weathering in a humid subtropical mountainous basin. *Chin. Sci. Bull.* **2011**, *56*, 3774–3782. [CrossRef]
5. Peng, H.; Liu, L.; Tao, Z.; Lv, X.; Li, S.; Deng, H.; Gao, Q. Chemical Weathering and Seasonal Variation of Chemical Compositions of Water in Humid Subtropical Basins—A Case Study for the Xizhijiang River Basin. *Earth Environ.* **2018**, *46*, 513–523.
6. Houghton, R.A. Balancing the Global Carbon Budget. *Annu. Rev. Earth Planet. Sci.* **2007**, *35*, 313–347. [CrossRef]
7. Rogelj, J.; Forster, P.; Kriegler, E.; Smith, C.; Séférian, R. Estimating and tracking the remaining carbon budget for stringent climate targets. *Nature* **2019**, *571*, 335–342. [CrossRef]
8. Sun, P.; Xiao, Q.; Guo, Y.; Miao, Y.; Wang, Q.; Zhang, C. Carbonate dissolution rate and karst carbon sink in mixed carbonate and silicate terrain: Take the upper reaches of the Lijiang river basin as an example. *Carsologica Sin.* **2021**, *40*, 825–834.
9. Zhang, C.; Xiao, Q.; Sun, P.; Gao, X.; Guo, Y.; Miao, Y.; Wang, J. Progress on karst carbon cycle and carbon sink effect study and perspective. *Bull. Geo. Sci. Technol.* **2022**, *41*, 190–198.
10. Zeng, C.; Liu, Z.; Zhao, M.; Yang, R. Hydrologically-driven variations in the karst-related carbon sink fluxes: Insights from high-resolution monitoring of three karst catchments in Southwest China. *J. Hydrol.* **2016**, *533*, 74–90. [CrossRef]
11. Li, Z.; Zhong, J.; Li, S.; Lang, Y.; Zhu, X.; Chen, S. The effects of hydrological variations on chemical weathering: Evidences from temporal water chemistry, stable carbon and sulfur isotopes. *Catena* **2022**, *214*, 106301. [CrossRef]
12. Ba, J.; Dan, Y.; Luo, F.; Tang, C.; Peng, C. Seasonal Differences in the Hydrochemical Characteristics of Karst Wetlands and the Associated Mechanisms in Huixian, China. *Water* **2022**, *14*, 2362. [CrossRef]
13. Li, J.; Xie, H.; Li, J.; Yang, G.; Xie, Y.; Wang, J.; Zhou, C.; Zou, S. Influences of anthropogenic acids on carbonate weathering and CO_2 sink in an agricultural karst wetland (South China). *Ecol. Indic.* **2023**, *150*, 110192. [CrossRef]
14. Liu, Z.; Dreybrodt, W.; Liu, H. Atmospheric CO_2 sink: Silicate weathering or carbonate weathering. *Appl. Geochem.* **2011**, *26*, S292–S294. [CrossRef]
15. Zhang, Y.; Yu, S.; He, S.; Sun, P.; Wu, F.; Liu, Z.; Zhu, H.; Li, X.; Zeng, P. New estimate of chemical weathering rate in Xijiang River Basin based on multi-model. *Sci. Rep.* **2021**, *11*, 5728. [CrossRef] [PubMed]
16. Qin, X.; Jiang, Z.; Zhang, L.; Huang, Q.; Liu, P. The difference of the weathering rate between carbonate rocks and silicate rocks and its effects on the atmospheric CO_2 consumption in the Pearl River Basin. *Geol. Bull. China* **2015**, *34*, 1749–1757.
17. Jiang, P.; Yu, G.; Zhang, Q.; Zou, Y.; Tang, Q.; Kang, Z.; Sytharith, P.; Xiao, H. Chemical weathering and CO_2 consumption rates of rocks in the Bishuiyan subterranean basin of Guangxi, China. *Sci. Rep.* **2020**, *10*, 11677. [CrossRef] [PubMed]
18. Guo, F.; Jiang, G.; Yuan, D.; Polk, J. Evolution of major environmental geological problems in karst areas of Southwestern China. *Environ. Earth Sci.* **2013**, *69*, 2427–2435. [CrossRef]
19. Pu, J.; Cao, M.; Zhang, Y.; Yuan, D.; Zhao, H. Hydrochemical indications of human impact on karst groundwater in a subtropical karst area, Chongqing, China. *Environ. Earth Sci.* **2014**, *72*, 1683–1695. [CrossRef]

20. Han, G.; Liu, C. Water geochemistry controlled by carbonate dissolution: A study of the river waters draining karst-dominated terrain, Guizhou Province, China. *Chem. Geol.* **2004**, *204*, 1–21. [CrossRef]
21. Xu, Z.; Liu, C. Chemical weathering in the upper reaches of Xijiang River draining the Yunnan-Guizhou Plateau, Southwest China. *Chem. Geol.* **2007**, *239*, 83–95. [CrossRef]
22. Perrin, A.-S.; Probst, A.; Probst, J.-L. Impact of nitrogenous fertilizers on carbonate dissolution in small agricultural catchments: Implications for weathering CO_2 uptake at regional and global scales. *Geochim. Cosmochim. Acta* **2008**, *72*, 3105–3123. [CrossRef]
23. Jiang, Y. The contribution of human activities to dissolved inorganic carbon fluxes in a karst underground river system: Evidence from major elements and $\delta^{13}C$(DIC) in Nandong, Southwest China. *J. Contam. Hydrol.* **2013**, *152*, 1–11. [CrossRef] [PubMed]
24. Guo, J.; Wang, F.; Vogt, R.; Zhang, Y.; Liu, C. Anthropogenically enhanced chemical weathering and carbon evasion in the Yangtze Basin. *Sci. Rep.* **2015**, *5*, 11941. [CrossRef] [PubMed]
25. Yu, S.; He, S.; Sun, P.; Pu, J.; Huang, J.; Luo, H.; Li, Y.; Li, R.; Yuan, Y. Impacts of anthropogenic activities on weathering and carbon fluxes: A case study in the Xijiang River basin, southwest China. *Environ. Earth Sci.* **2016**, *75*, 589. [CrossRef]
26. Sun, P.; He, S.; Yuan, Y.; Yu, S.; Zhang, C. Effects of aquatic phototrophs on seasonal hydrochemical, inorganic, and organic carbon variations in a typical karst basin, Southwest China. *Environ. Sci. Pollut.* **2019**, *26*, 32836–32851. [CrossRef]
27. Zhang, L.; Qin, X.; Liu, P.; Huang, Q. Chemical denudation rate and atmospheric CO_2 consumption by H_2CO_3 and H_2SO_4 in the Yangtze river catchment. *Acta Geol. Sin.* **2016**, *90*, 1933–1943.
28. Huang, Q.; Qin, X.; Liu, P.; Zhang, L.; Su, C. The Influence of Allogenic Water and Sulfuric Acid to Karst Carbon Sink in Karst Subterranean River in Southern Hu'nan. *Adv. Earth Sci.* **2017**, *32*, 307–318.
29. Xie, Y.; Huang, F.; Yang, H.; Yu, S. Role of anthropogenic sulfuric and nitric acids in carbonate weathering and associated carbon sink budget in a karst catchment (Guohua), southwestern China. *J. Hydrol.* **2021**, *599*, 126287. [CrossRef]
30. Zhao, J. Research on Geological Disaster Development Characteristics and Formation Conditions in Yingde City, Guangdong Province. *Ground Water* **2018**, *40*, 108–109.
31. Chen, X.; Zhang, J.; Xiang, H.; Wei, H. Study on the changing trend of acid rain in Guangdong province from 2008 to 2018. *J. Ecol. Environ.* **2020**, *29*, 1198–1204.
32. Ward, J. Hierarchical grouping to optimize an objective function. *J. Am. Stat. Assoc.* **1963**, *69*, 236–244. [CrossRef]
33. Pang, Z.; Kong, Y.; Li, J.; Tian, J. An Isotopic Geoindicator in the Hydrological Cycle. *Prog. Earth Planet Sc.* **2017**, *17*, 534–537. [CrossRef]
34. Piper, A.M. A graphic procedure in geochemical interpretation of water analyses. *Eos Trans. Am. Geophys. Union* **1944**, *25*, 914–923.
35. Huang, Q.; Qin, X.; Cheng, R.; Li, T. Hydrochemical characteristics and control factors of karst hyporheic zones in the karst peak forest region of the middle reaches of the Zuo River. *Hydrogeol. Eng. Geol.* **2019**, *46*, 1–8.
36. Sun, P.; Yu, S.; Mo, F.; He, S.; Lu, J.; Yuan, Y. Hydrochemical Characteristics and Influencing Factors in Different Geological Background: A Case Study in Darongjiang and Lingqu Basin, Guangxi, China. *Environ. Sci.* **2016**, *37*, 123–131.
37. Nguyen, T.; Park, M.; Son, J.; Choi, S. Spatial distribution and temporal variation of polycyclic aromatic hydrocarbons in runoff and surface water. *Sci. Total Environ.* **2021**, *793*, 148339. [CrossRef]
38. Moquet, J.; Crave, A.; Viers, J.; Seyler, P.; Armijos, E.; Bourrel, L.; Chavarri, E.; Lagane, C.; Laraque, A.; Casimiro, W.; et al. Chemical weathering and atmospheric/soil CO_2 uptake in the Andean and Foreland Amazon basins. *Chem. Geol.* **2011**, *287*, 1–26. [CrossRef]
39. Xie, Y.; Yang, Q.; Liao, P.; Sun, Y.; Gao, Q. A Review of the Effects of Chemical Weathering with Sulfuric Acid on River Hydrochemistry in Hot and Humid Catchment. *Earth Environ.* **2022**, *50*, 537–546.
40. Li, D.; Zhang, L.; Li, C.; Wang, X.; Wang, X.; Yang, Z.; Qin, L. Quantitative analysis of dissolved inorganic carbon sources in water bodies in the Lujiang river basin. *Carsologica Sin.* **2024**, *43*, 92–104.
41. Gaury, K.P.; Meena, N.K.; Mahajan, A.K. Hydrochemistry and water quality of Rewalsar Lake of Lesser Himalaya, Himachal Pradesh, India. *Environ. Monit. Asses.* **2018**, *190*, 84. [CrossRef] [PubMed]
42. Huang, G.; Sun, J.; Zhang, Y.; Chen, Z.; Liu, F. Impact of anthropogenic and natural processes on the evolution of groundwater chemistry in a rapidly urbanized coastal area, South China. *Sci. Total Environ.* **2013**, *463-464*, 209–221. [CrossRef]
43. Rafighdoust, Y.; Eckstein, Y.; Harami, R.; Gharaie, M.; Mahboubi, A. Using inverse modeling and hierarchical cluster analysis for hydrochemical characterization of springs and Talkhab River in Tang-Bijar oilfield, Iran. *Arab. J. Geosci.* **2016**, *9*, 241. [CrossRef]
44. Khanday, S.; Romshoo, S.; Jehangir, A.; Sahay, A.; Chauhan, P. Environmetric and GIS techniques for hydrochemical characterization of the Dal lake, Kashmir Himalaya, India. *Stoch. Env. Res. Risk. A* **2018**, *32*, 3151–3168. [CrossRef]
45. Wang, Z.; Jia, D.; Song, S.; Sun, J. Assessments of surface water quality through the use of multivariate statistical techniques: A case study for the watershed of the Yuqiao Reservoir, China. *Front. Environ. Sci.* **2023**, *11*, 1107591. [CrossRef]
46. Gibbs, R.J. Mechanisms controlling world water chemistry. *Science* **1970**, *170*, 1088–1090. [CrossRef]
47. Marandi, A.; Shand, P. Groundwater chemistry and the Gibbs Diagram. *Appl. Geochem.* **2018**, *97*, 209–212. [CrossRef]
48. Galy, A.; France, L.C. Weathering processes in the Ganges-Brahmaputra basin and the riverine alkalinity budget. *Chem. Geol.* **1999**, *159*, 31–60. [CrossRef]
49. Gaillardet, J.D.B.L.; Dupré, B.; Louvat, P.; Allegre, C.J. Global silicate weathering and CO_2 consumption rates deduced from the chemistry of large rivers. *Chem. Geol.* **1999**, *159*, 3–30. [CrossRef]
50. Xie, Y.; Yu, S.; Miao, X.; Li, J.; He, S.; Sun, P. Chemical weathering and its associated CO_2 consumption on the Tibetan Plateau: A case of the Lhasa River Basin. *Earth Sci. Front.* **2023**, *30*, 510–525.

51. Wu, J.; Wang, L.; Gong, F.; Ye, T. Genesis and Mineralization of Granite in Hongling Tungsten Deposit in Northern Guangdong. *Geotecton. Et Metallog.* **2023**, *47*, 695–710.
52. Huang, Q.; Qin, X.; Liu, P.; Zhang, L.; Su, C. Impact of sulfuric and nitric acids on carbonate dissolution, and the associated deficit of CO_2 uptake in the upper-middle reaches of the Wujiang River, China. *J. Contam. Hydrol.* **2017**, *203*, 18–27. [CrossRef] [PubMed]
53. Zhu, H.; Wu, L.; Xin, C.; Yu, S.; Guo, Y.; Wang, J. Impact of anthropogenic sulfate deposition via precipitation on carbonate weathering in a typical industrial city in a karst basin of southwest China: A case study in Liuzhou. *Appl. Geochem.* **2019**, *110*, 104417. [CrossRef]